Research Square

Preprints are preliminary reports that have not undergone peer review.
They should not be considered conclusive, used to inform clinical practice,
or referenced by the media as validated information.

# Global Patterns of Soil Freeze-Thaw States Below 0 °C

**Yuanchao Fan**

yuanchao.fan@sz.tsinghua.edu.cn

Tsinghua University https://orcid.org/0000-0002-3462-1820

**Zhaoyu Dong**

**Article**

**Keywords:**

**Posted Date:** July 31st, 2026

**DOI:** https://doi.org/10.21203/rs.3.rs-10410001/v1

**License:** This work is licensed under a Creative Commons Attribution 4.0 International License.
Read Full License

**Additional Declarations:** There is **NO** Competing Interest.

# Abstract

Current climate models assume that soil freezes at 0°C, neglecting freezing-point depression caused by dissolved salts and matrix effects—a long-recognized but poorly quantified mechanism at large scales. Here, we integrate freeze-thaw states and soil temperature records from Soil Moisture Active Passive (SMAP) satellite observations with soil property datasets to characterize sub-zero unfrozen soil (SUS) events and quantify the freezing-point depression effect across the Northern Hemisphere. Using 137,554 SMAP pixels spanning 2015–2022, we estimate a median soil freezing point of 271.50 K for nocturnal freezing events, approximately 1.65°C below that of pure water. SUS events have a wide range of occurrence temperatures (interquartile range: 269.04–272.74 K), with 48.79% occurring below the median freezing point. Machine learning analysis reveals that these low-temperature events are primarily driven by soil salinity and the spontaneous thermodynamic character of thawing. Validation against 19 collocated FLUXNET eddy-covariance sites shows that SMAP-derived (271.65 K) and in-situ (272.01 K) median freezing points differ by only 0.36 K, with no statistically significant difference between their distributions. These findings indicate that the 0°C assumption in Earth system models systematically underestimates permafrost thaw onset and degradation risks, with critical implications for carbon-climate feedbacks from permafrost regions.


# Introduction

The soil freeze-thaw process plays a vital role in regulating the energy and water cycles in cold regions[1,2]. Permafrost is highly sensitive to climate change[3–5], and its degradation triggers cascading effects – including water depletion and carbon release – that will profoundly affect geophysical processes while amplifying the positive feedback mechanism in global climate system[6–8].

The freezing point of soil pore water is influenced by multiple factors, including soil water content, mineral composition, pore water salinity, pore size, and soil plasticity[9–12]. Traditionally, it is believed that soil freezing needs to go through a supercooling stage, followed by an equilibrium freezing point (Supplementary Fig. 1). Salt increases the nucleation barrier of the soil-water system by providing Gibbs free energy, thereby reducing the freezing point[13]. This reduction effect turns into a nonlinear effect when the number of solute types increases[14–16]. The freezing point is often regarded as the boundary between freezing and thawing[15,16]. Researchers have developed very sophisticated thermos-hydro-mechanical-chemical models based on laboratory control experiments and numerical methods[17–19]. However, these models rely heavily on detailed soil boundary conditions, complex parameters and high-precision salinity data, creating scale barriers in the application of microscopic mechanisms to macroscopic physical models. These barriers result in a methodological asymmetry between fine-scale laboratory simulations and large-scale theoretical and modelling studies, the latter still resorting to simplified algorithms for determining soil freeze-thaw states[20–25]. For example, the theoretical model of Niu and Yang[26] is the core of the Community Land Model (CLM)'s freeze-thaw distinction which simulates soil physical effects (porosity and absorptivity) on the maximum amount of supercooled soil

water below 0°C, but the freezing point and associated energy fluxes are still determined by 0°C. Substantial biases exist between modeled and observed soil moisture in soil freezing process simulated by this scheme. Notably, such simplifications vary significantly across Earth system models; while most schemes fix the freezing point at 0°C, some—such as the GFDL models—apply a constant offset (e.g., -2°C) to implicitly account for the freezing-point depression effect[27]. However, these prescribed thresholds fail to capture the complex spatiotemporal variability of the sub-zero unfrozen state. To mitigate this issue, Yang et al.[28] implemented in CLM4.5 a flexible freezing point that varies based on phase change efficiency – a parameter representing how soil ice and liquid water content and soil temperature collectively influence the rate of soil phase change. Although this scheme improved the relationship between soil moisture and temperature, biases remain due to the neglection of other physical and chemical interactions in the soil. Building on a different approach, Li et al.[29] incorporated a semi-implicit, physics-based scheme of soil freeze–thaw processes into the SSiB3 land surface model to ensure thermodynamic equilibrium between ice and liquid water based on enthalpy and water mass conservation. However, the freezing-point depression effect caused by dissolved solutes was not considered, leaving a key physicochemical mechanism unresolved in Earth system modelling. Wu et al.[30] successfully implemented a salt-induced freezing-point depression function in CoupModel and demonstrated improved performance in reproducing soil temperature dynamics in saline frozen soils of northern China, yet such advances have not been implemented in large-scale Earth system models. The neglection of the freezing point depression caused by soil salinity in Earth system models might contribute to the underestimation of permafrost degradation rates in response to climate change[31,32]. The above gaps in Earth system modelling are partly due to the lack of large-scale observation-based quantification of the freezing-point depression effect associated with sub-zero unfrozen states in global freeze-thaw active zones.

Researchers have explored many alternative methods to monitor soil freeze-thaw status, bypassing temperature-based identification, but technologies such as time domain reflectometry, heat pulse method, and nuclear magnetic resonance method are limited by high monitoring costs and limited spatial scales[33,34]. With the development of satellite remote sensing technology, passive and active remote sensing methods have provided long time series of high-precision soil property data. The advent of radar and microwave radiometers has enabled extensive long-term measurement of soil dielectric properties, which becomes an efficient means for soil freeze-thaw state identification without reliance on soil temperature. Various satellite radiometers and scatterometers operating at different frequencies have been employed to detect soil freeze-thaw states. The L-band radar demonstrates superior soil penetration depth and sensitivity. Notable products include the Soil Moisture Active Passive (SMAP) satellite mission, the Soil Moisture and Ocean Salinity (SMOS) mission, and the Advanced Microwave Scanning Radiometer-2 (AMSR-2). The SMAP mission provides data on soil moisture and freeze-thaw states based on dielectric constant variations reflected by the normalized polarization ratio of microwave radiometers, demonstrating high accuracy on a global scale[35,36]. In addition, near-surface soil temperature is derived by assimilating SMAP soil moisture retrievals into a land surface model, ensuring physical consistency with hydrological and thermal dynamics.

In this study, we use satellite radar remote sensing data and eddy covariance flux tower data to explore the spatiotemporal patterns and driving factors of soil freeze-thaw below 0°C and to quantify the freezing-point depression effect of soil properties and identify soil freezing points under realistic field conditions. We develop an integrated geospatial dataset by leveraging 137,554 grid cells (at 9-km spatial resolution) exhibiting intensive freeze-thaw dynamics across the Northern Hemisphere, synergizing soil property parameters with SMAP satellite records spanning 2015–2022. The dataset incorporates 12-hourly resolved freeze-thaw state classifications coupled with hourly soil hydrothermal variables. We use this dataset to analyze the effects of multiple physical and chemical factors on soil freeze-thaw dynamics under conditions below 0°C, and determine the occurrence temperature distribution of sub-zero unfrozen state (SUS) events and soil freezing points. We further estimate the soil freezing points under realistic field conditions using flux tower observations and compare them with the soil freezing points retrieved from satellite data. The results have significant implications for future Earth system model development and large-scale monitoring and forecasting of permafrost degradation and associated greenhouse gases emissions and ecosystem changes.

## Results

# Spatiotemporal and temperature characteristics of SUS events

Our analysis of SUS event occurrence during 2015–2022 reveals a bimodal seasonal pattern (Fig. 1a-c), with the primary peak during the thawing season (February-May) and secondary peak during the freezing season (October-January). The occurrences of SUS events during the thawing season surpass those in the freezing season by 13.43% (n = 9,042,137/y, Supplementary Table 1) and demonstrate a persistent seasonal asymmetry across different datasets (Fig. 1c with SMAP soil temperature and freeze–thaw state data; Supplementary Fig. 2 with ERA5 soil temperature data).

All SUS events constitute 31.59% of sub-zero soil temperature conditions annually, with monthly proportions ranging from 14.09% (January) to 79.40% (May) (Fig. 1e). The frequency of SUS events peaks in April, averaging 29 occurrences per sampling site monthly, corresponding to intensified soil phase transitions during the spring thawing period. The longest continuous SUS event persisted for an average of 11 days, spanning 22 data recording intervals. We classify SUS events into four categories based on phase change characteristics (see Methods “Definition of freeze-thaw events”). Among these categories, consistent thawing (CT) events dominate across seasons, while thawing process (TP) and freezing process (FP) events exhibit strong seasonal and diurnal asymmetries (see Supplementary Supporting Text 1).

Noticeable differences in the occurrence soil temperatures of SUS events are observed across different time scales and seasons. Specifically, SUS events predominantly occur at soil temperatures above 263 K, representing 94.8% of the dataset, with an average occurrence temperature of 270.10 K and an interquartile range (IQR) of 269.04–272.74 K (5th – 95th percentile range of 262.97–273.12 K) (Fig. 2a).

Overall, SUS events occurring at 18:00 tend to have higher soil temperatures and lower standard deviations than those at 6:00 (Supplementary Table 1).

Spatial heterogeneity in SUS event occurrence is evident, with regional variations in occurrence temperature characterized by a standard deviation of 3.6 K. Figures 2b and 2d highlight that relatively low SUS event temperatures and high occurrence frequencies are concentrated in the Mongolian Plateau, eastern Russia, and northwestern Alaska/Canada, where their occurrence soil temperatures also exhibit higher standard deviations (Fig. 2f). A comparison of the distributions of annual occurrence frequencies between SUS and Above-zero Frozen State (AFS) events shows that there are very few (abnormal) AFS events across the Northern Hemisphere (mean ratio of 1:24 relative to SUS events) except for the Tibetan Plateau (Supplementary Fig. 3). The limited fraction of AFS events and no apparent spatial heterogeneity in above-mentioned regions (Supplementary Fig. 3d) with low SUS occurrence temperatures (Fig. 2b) suggest that data uncertainties could only explain a minor portion of soil temperature variations in all events. Therefore, the notable spatial patterns of SUS events and their occurrence temperatures most likely reflect viabilities in the driving factors of SUS (such as soil moisture and salinity analyzed in the next section).

## Quantification of drivers

The observed spatiotemporal characteristics and heterogeneous occurrence temperatures of SUS events necessitate the isolation of their potential drivers. We employed the XGBoost machine learning model to investigate the driving factors of SUS events (classification model) and to quantify the contributions of various predictors to the SUS occurrence temperatures (regression model; see Methods section “XGBoost framework”) at two different time points (6:00 and 18:00). A total of 14 features were incorporated into both models, including temperature-related indicators: Soil–Surface Temperature Difference (SSTD), Hours Below 0°C (HB0C), Soil Temperature Time Derivative (STTD), and Soil Temperature Change Rates at 1, 6, and 12 hours (ST1RC / ST6RC / ST12RC); soil condition indicators: Soil Moisture (SM), Cation Exchange Capacity (CEC), Soil Organic Carbon (SOC), and soil particle composition (Clay / Silt / Sand); and seasonal indicators: sine and cosine transformations of the calendar month (M_sin / M_cos). Both classification and regression models demonstrate robust performance. Classification models achieve 0.99 of the metric AUC-ROC (Area Under the Receiver Operating Characteristic Curve; see Methods section “XGBoost framework”) and regression models explain 93% of variance ($R^2$=0.93, $p < 0.01$; Supplementary Table 2).

In the classification model, SSTD demonstrates the highest variable importance at both time points, with the SHAP importance value (4.79) nearly equal to the sum of all other features (4.84) at 18:00 (Supplementary Figs. 4a, b for mean feature importance ranking; 5a, b for feature contribution summary). Beyond temperature metrics, the cation exchange capacity (CEC), indicative of soil salinity, emerges as the most influential feature for the occurrence of SUS events across both time points (Supplementary Figs. 4a, b and 5a, b). The quantification of feature contributions (Fig. 3c for all SUS events; Supplementary Fig. 6c, f for 6:00 and 18:00 SUS events, respectively) shows that the net

contribution of increased CEC is to promote the occurrence of SUS events. Figure 3d illustrates that this effect is only evident above a CEC concentration threshold of 40 cmol(+)/kg and exhibits a nonlinear relationship, where the effect becomes saturated when CEC is greater than 80 cmol(+)/kg, consistent with other studies[37].

In the regression model, seasonal and temperature features (such as M_cos, M_sin, HB0C and ST12RC) exhibit the most dominant influences on the prediction of SUS occurrence temperatures (Supplementary Figs. 4c, d and 5c, d). After accounting for seasonal variations and temperature metrics, soil moisture (SM) emerges as the most prominent feature in importance ranking (Supplementary Figs. 4c, d and 5c, d). As shown in Fig. 3g, the predominance of negative relative to positive SHAP values suggests that the net effect of increasing SM is to lower the occurrence temperature of SUS events (Supplementary Fig. 6i, l for 6:00 and 18:00 SUS events, respectively). This freezing point depression effect is only evident when SM content is below 0.25 and is more pronounced at lower SM levels (Fig. 3h). This threshold-dependent behavior reflects critical hydrological thresholds in the soil-water system's thermal regulation mechanisms[14,38]. In both models, Clay and Silt are key driving factors of SUS events and lead to lower occurrence temperatures of SUS events, which is consistent with previous studies, because the smaller the soil pore size, the stronger water absorptive strength and the lower the minimum supercooling temperature[39,40].

Comparison of soil temperature and surface (skin) temperature records associated with FP (freezing) and TP (thawing) types of SUS events reveals distinct thermal regimes between nighttime and daytime freeze-thaw processes (Supplementary Supporting Text 2). Despite the distinct thermal regimes, the binned data analysis reveals a consistent influence of SM and CEC across both processes. For both FP and TP SUS events, mean soil temperatures converged near 0°C under conditions of relatively high SM and low CEC levels (Supplementary Fig. 7b–c, f–g). Conversely, SUS events with lower soil temperatures (below 0°C) occurred more frequently under conditions of relatively low SM and high CEC. A distinct clustering of low mean soil temperatures emerged when CEC concentrations approached 40 cmol(+)/kg (Supplementary Fig. 7b–c, f–g), corroborating the role of CEC identified in the machine learning analysis (Fig. 3d).

## Observation-derived soil freezing points

The widespread occurrences of sub-zero freeze-thaw dynamics shown in the above analysis motivate us to identify true freezing point soil temperatures. There are two instances during the soil freezing process when the tangent of soil temperature-time curve is horizontal. The first occurs when the free water in the soil reaches the critical nucleation state, and the soil temperature at this point is the minimum supercooling temperature ($T_{sc}$)[40,41] (see schematic in Supplementary Fig. 1). The second happens when all latent heat has been released by the soil's free water, and the soil-water system reaches equilibrium freezing temperature ($T_f$, also referred to as soil freezing point[40], at which point the capillary water begins to freeze in a steady-state process. Hourly soil temperature data from a sample region clearly

shows the presence of these two critical points with horizontal tangents, indicating $T_{sc}$ and $T_f$, during the freezing process (the twelve hours before the frozen state; Supplementary Figs. 8a, b, and 9). The difference between $T_f$ and $T_{sc}$ reflects the mean magnitude of latent heat release during freezing at each grid point. In contrast, the thawing process does not have a steady-state or change point for determining the initiation of thawing (schematic in Supplementary Fig. 1 and data in Supplementary Fig. 8c, d) due to the spontaneity of the thawing process and the pre-thawing mechanism of ice[42]. Thus, most studies on the freezing point primarily focused on detecting $T_f$ in the freezing process[42,43].

By quantitatively matching the supercooling and latent heat release processes of the soil temperature curve during soil freezing, we obtained the spatial (Supplementary Fig. 10a, b) and statistical (Supplementary Table 3) distribution of $T_f$ in the Northern Hemisphere using satellite data (Methods section "Determination of $T_f$ and $T_{sc}$ using SMAP"). The median $T_f$ is 271.50 K (mean: 270.28 ± 3.36 K) for FP events at 18:00 (nocturnal freezing occurred during 18:00–6:00) (Supplementary Table 3). For FP events at 06:00 (daytime freezing during 6:00–18:00), the median $T_f$ is 271.03 K (mean: 269.62 ± 4.04 K), which is lower than that observed at 18:00. The difference between $T_f$ and $T_{sc}$ indicates latent heat release during freezing, which is significantly lower for nocturnal freezing process (median $T_f$ -$T_{sc}$ = 0.13 K; Supplementary Table 3; Fig. 10c, d) compared to daytime freezing (median $T_f$ -$T_{sc}$ = 0.87 K; Supplementary Table 3). The larger $T_f$ -$T_{sc}$ during daytime is likely attributable to the coincidence of latent heat release with solar radiation in the day. To minimize the potential influence of solar radiation on soil temperature dynamics during freezing, we therefore focus on $T_f$ derived from nocturnal freezing events, using only 18:00 FP events in subsequent analyses.

Using half-hourly in-situ observations from 19 FLUXNET eddy covariance flux towers, we identify soil freezing events and associated $T_f$ and $T_{sc}$ through a multi-criteria diagnostic framework that integrates the coupled dynamics of soil heat flux, soil temperature and moisture (see Methods: Determination of $T_f$ and $T_{sc}$ using in-situ observations). The in-situ derived median soil freezing point is 272.01 K (mean: 270.24 ± 3.85 K; Supplementary Table 4) for the top layer (~ 5 cm, consistent with SMAP satellite data). Due to the stochastic nature of the timings of $T_f$ and $T_{sc}$, we use the time interval between them as a grouping variable and compute median soil temperature evolution curves for intervals of 3, 3.5, 4, and 4.5 hours (Supplementary Figs. 11 and 12). These subsets account for nearly 70% of the total in-situ samples (Supplementary Fig. 12). Consistent temperature fluctuation characteristics are also observed across various soil depths; notably, the mean $T_f$ exhibits a systematic increase with soil depth (i.e., higher/warmer freezing point for deeper soil layer; Supplementary Fig. 13).

To validate the satellite-derived freezing points, we compared $T_f$ estimates from 19 SMAP pixels collocated with the flux tower sites and found close agreement between the two data types. Specifically, the SMAP-derived median and mean $T_f$ values are 271.65 K and 270.81 K, respectively (Fig. 4a), with the SMAP median 0.36 K lower and the SMAP mean 0.56 K higher than their in-situ counterparts (median: 272.01 K; mean: 270.24 K) (Supplementary Table 4). The kernel density estimation (KDE) curves of

satellite- and in-situ-derived $T_f$ are closely aligned, with modal values differing by only 0.2 K (272.57 K for SMAP vs. 272.37 K for in-situ observations) (Fig. 4a; Supplementary Table 4). Statistical tests confirm no significant differences between the two datasets at the 0.05 significance level, both in distributional characteristics (Kolmogorov-Smirnov (K-S) test: $p = 0.0648$) and in mean values (Welch's t-test: $p = 0.0522$). At the site level, the finer temporal resolution of in-situ soil temperature and heat flux records enables identification of a greater number of freezing events than satellite retrievals across most stations (circle size in Fig. 4b indicates $T_f$ sample counts). When these $T_f$ values are temporally averaged at each SMAP pixel and at the corresponding flux tower site, both the scatterplot and the map reveal that in-situ site-averaged $T_f$ is higher (warmer) than that of the collocated SMAP pixel at most stations (Fig. 4b, c). Although our multi-criteria hydrothermal $T_f$ diagnostic framework utilizes all available in-situ data (Methods section "Determination of $T_f$ and $T_{sc}$ using in-situ observations"), the absence of direct freeze-thaw state monitoring in flux-tower sites poses an inherent limitation to this remote sensing – in situ comparison (see Discussion).

# Discussion

Current soil freeze-thaw schemes in climate models have limited ability to simulate freezing point depression effects due to poorly constrained physicochemical mechanisms. Limited observational data further hinder the characterization of metastable phase transitions influenced by soil physical and chemical conditions. This paper presents a comprehensive machine learning and statistics-based assessment of soil freeze-thaw dynamics and sub-zero freezing point identification in the Northern Hemisphere using SMAP satellite data supplemented by flux tower observations. We find a median soil freezing point nearly 1.65°C lower than the theoretical freezing point of pure water, derived from satellite data and cross-validated by in-situ observations. The freezing point depression effect can be largely attributed to the interplay between soil salinity and soil water content. These two soil properties are key explanatory variables for the occurrence of SUS events in our machine learning model. We find that 48.79% of SUS events occurred at soil temperatures below the median observed $T_f$ (271.50 K) and 47.17% even occurred below the median observed $T_{sc}$ (271.38 K). Moreover, SUS events spanned a broad temperature range (IQR of 269.04–272.74 K), with low-temperature SUS events primarily attributed to the presence of unfrozen water and premature thawing processes occurring in the soil. Our results suggest potentially underestimated active layer thawing rates and permafrost degradation risks by current climate models.

We find a marked asymmetry in the frequency and soil temperature distribution of SUS events during freeze-thaw cycles, primarily due to the thermodynamic irreversibility of freezing and thawing processes. During freezing, the soil experiences a supercooling state which causes the freezing temperature curve to be delayed (referred to as hysteresis) relative to the thawing temperature curve[40,44], resulting in higher occurrence temperatures of the freezing process. Thawing process SUS events occur more frequently in months when ambient temperatures warm up and exhibit significantly different diurnal freeze-thaw patterns than those of the freezing process. Although the latent heat released and absorbed during

freezing and thawing is the same, the freezing process requires additional energy release to overcome the nucleation energy barrier before it can begin. In contrast, thawing is a spontaneous, entropy-increasing process[45], where the absorbed thermal energy disperses as latent heat (for phase change), which weakens the lattice binding forces and allows molecules to depart from the solid structure, rather than reaching a nucleation threshold[43]. This spontaneous character of the thawing process leads to larger uncertainty in its occurrence temperatures across seasons. This interpretation is also supported by the observation that nighttime thawing occurs at significantly lower temperatures than daytime thawing.

The higher frequency of SUS events during the thawing process can also be attributed to variations in solar radiation and soil salinity, in addition to the aforementioned spontaneous nature of the entropy-increasing process[45]. Under controlled laboratory conditions, energy transfer typically occurs solely through temperature gradients from a warmer surface to cooler deeper layers[38,40,46,47]. However, in real-world conditions, the majority of thawing-process (TP) type SUS events occurred when surface (skin) temperatures were lower than the subsurface soil temperatures (Supplementary Fig. 8c). This indicates additional heat source likely originating from deeper soil layers, but we lack observations of deeper soil temperatures to verify this hypothesis. Moreover, some studies suggest that soil moisture content interacts with soil salinity in determining the freezing point[37,48,49,50]. As the thawing process progresses, the soil solution becomes more diluted, reducing the salt-induced depression of the freezing point as CEC content decreases. Consequently, the occurrence temperature of thawing is also unlikely to remain constant across regions and seasons and even during a single SUS event.

Nighttime freezing process, in particular, carries relatively lower retrieval uncertainty, enabling us to identify $T_f$ based on soil temperature dynamics and freeze-thaw states from satellite data, corroborated by coupled signals of energy flux and soil hydrothermal dynamics from flux tower measurements. The occurrence of low-temperature refreezing processes likely contributes to the lower tails of both satellite and in-situ derived $T_f$ distributions. Notably, the KDE peak freezing point temperatures estimated from satellite data and in-situ measurements match closely with each other, demonstrating the feasibility and validity of large-scale satellite-based retrieval of sub-zero soil freezing dynamics. The nuanced differences between satellite- and in-situ-derived $T_f$ estimates arise naturally from their distinct data sources and estimation approaches: in-situ observations capture the most probable physical freezing onset at the soil micro-scale, while satellite-based estimates reflect spatially and temporally aggregated freeze–thaw states. Importantly, despite this aggregation—which inherently tends to smooth the data distributions—the satellite-based approach successfully preserves the modal freezing temperature without shifting the overarching thermal distribution (Fig. 4a). Furthermore, consistent thermal signatures and freezing point dynamics are discernibly detected in deeper soil layers, reinforcing the physical robustness of these subsurface freezing processes (Supplementary Figs. 11–13). Moreover, the absence of ancillary freeze-thaw state labels in in-situ records may unavoidably lead to misidentification of subsequent cooling processes within an already frozen state as initial freezing events, thereby resulting in anomalously lower $T_f$ values in the tail of the in-situ $T_f$ distribution.

The distinct characteristics of SUS events and sub-zero soil freezing points reveal a critical but underappreciated vulnerability in permafrost thermal regimes. By incorporating the physics of soil freezing point depression into our multi-source diagnostic framework, we demonstrate that the initiation of permafrost thawing in the Northern Hemisphere could occur 1 to 2°C earlier than projected by models assuming a conventional 0°C freezing threshold[51,52]. We emphasize that this advance primarily concerns the onset of thawing, not necessarily a proportional increase in long-term vertical degradation rates: the total enthalpy required to thaw a permafrost column is governed largely by its ice content and depth — quantities already partially constrained by satellite estimates — and these are not substantially altered by the freezing point depression itself. However, the temporal shift in thaw initiation carries its own significance. Sub-zero liquid water modifies latent heat partitioning and increases near-surface thermal conductivity, expanding the period of thermal activity during freeze–thaw transitions even when bulk soil temperatures remain below 0°C. Critically, these conditions — unfrozen soil water at sub-zero temperatures — give rise to biogeochemically active states that current Earth system models, anchored to a 0°C freezing threshold, systematically fail to represent; microbial decomposition of soil organic carbon can proceed at temperatures well below 0°C in the presence of liquid water, a process invisible to models that treat such soils as frozen. While the degree to which this mechanism amplifies permafrost-climate feedbacks at decadal or longer timescales remains an important open question, the earlier onset of these processes is observationally supported and consequential: given the 1.1°C of warming already recorded, a 1–2°C advance in thaw initiation substantially erodes — and in many regions may already exceed — the remaining temperature budget of less than 0.9°C implied by the Paris Agreement's 2°C target[53,54]. The thermally and hydrologically prolonged transitional state indicated by the SUS events and subzero freezing points may represent greater permafrost vulnerability than previously recognized and precondition northern ecosystems for broader hydroclimatic and carbon-cycle feedbacks[55]. Therefore, the integration of realistic freeze-thaw parameterizations into Earth system models is essential to reduce the underestimation of early-stage permafrost vulnerability and to better reconcile model projections with satellite and in-situ observations.

A limitation of this study comes from inherent uncertainties in satellite data and the lack of in-situ observations to calibrate satellite (SMAP)-derived frozen state classification. While monitoring stations provide continuous data on soil hydrothermal conditions, long-term observational networks for soil freeze-thaw states still rely on temperature metrics, which may cause marked mismatches with satellite-derived freeze-thaw states based on radar signals. In the QLB-NET soil moisture and freeze–thaw monitoring network, researchers found that increasing the number of in-situ monitoring sites enhances the consistency between SMAP satellite estimates and the in-situ classification of freeze-thaw states, but inconsistency remains high during the frozen/thawed transition seasons (e.g., March, April, October, and November) due to the existence of SUS events recorded by SMAP but overlooked by in-situ classification of freeze-thaw states based on a definitive 0°C threshold[56]. Similarly, in the SMN-WDL permafrost observation network, temperature-focused permafrost classification still relies on the 0°C threshold, with most misclassifications in thaw state occurring between 0°C and − 5°C[36]. This also reflects a subjective neglection of SUS events.

Furthermore, the precise quantification of salinity's role in soil freezing point of SUS events and the comparative assessment of latent heat release versus solar radiation impacts on soil thermal dynamics are currently constrained by the coarse resolution of available datasets in this investigation. The estimation of actual soil freezing points is based on 3-hourly variations in soil temperature within 12-hour freeze-thaw windows. However, due to limited temporal resolution, substantial latent heat release may occur within 3-hourly observation intervals, which cannot be fully captured. Some regions such as the Tibetan Plateau show relatively large uncertainty in the occurrence of SUS and AFS events. The higher temperature sensitivity of high-latitude regions to warming would exacerbate the impact of climate change on freeze-thaw dynamics and permafrost degradation[57,58]. The seasonal distribution of SUS events reveals the possible existence of a "year-round window" for soil microbial activity. The hidden thaw beneath frozen surfaces warrants further assessment of permafrost-climate feedbacks. Consequently, there is an urgent need for an integrated, multi-dimensional observational framework to comprehensively evaluate soil freezing processes, which would enable more precise quantification of soil freezing point dynamics across diverse spatio-temporal scales.

In summary, this study demonstrates widespread sub-zero freeze-thaw cycles in the Northen Hemisphere, which is co-regulated by soil moisture and salinity thresholds. The prevalence of SUS events could promote microbial activity year-round, turning cold soils into stealthy carbon sources. The mechanisms shown in this study explain at least partially why permafrost degradation outpaces model projections[59]. Permafrost is no longer a dormant carbon vault but a ticking clock[7]. The potential increasing frequency of SUS events under further warming could tip the Arctic region over a threshold, leading to more pronounced non-linear carbon release and intensified land-atmosphere feedbacks — a systematic risk that current climate commitments fail to encapsulate, thereby highlighting the urgent need for enhanced climate mitigation efforts[54].

## Materials and Methods

# Study area and soil property data

Based on the statistical analysis of SMAP L3 freeze-thaw status and SMAP L4 soil temperature and surface (skin) temperature data (Supplementary Table 5) over the entire time span, a total of 1,067,338 grid points (9-km resolution) with valid records were identified. To ensure consistency in seasonal patterns and the reliability of freeze-thaw retrievals, the following criteria were applied: Southern Hemisphere records were excluded to maintain uniform seasonal representation. Grid points with > 1% missing data were filtered out to ensure continuous freeze-thaw state monitoring. Grid cells were excluded if their multi-year average surface temperature exceeded 0°C or exhibited long-term frozen conditions, focusing on active freeze-thaw processes. Finally, grid points with annual mean soil temperatures between − 5°C and 0°C were retained to better capture the freeze-thaw dynamics, thereby facilitating effective analysis of these processes. This resulted in 137,554 valid grid points, primarily

located between 25°N and 75°N, covering the Tibetan Plateau, Mongolian Plateau, Alaska, northern Canada, parts of northern Europe, and parts of Siberia in Russia.

Soil particle gradation (Sand, Silt, Clay), permanent wilting point (PWP), soil organic carbon (SOC), and cation exchange capacity (CEC) data were obtained from SoilGrids, a global digital soil mapping system that utilizes advanced machine learning techniques to delineate the spatial distribution of soil properties worldwide. The outputs consist of global soil property maps at six soil depth intervals and a spatial resolution of 1,000 meters. For this study, data from the 0–5 cm depth were used for subsequent analysis[60,61].

## SMAP freeze-thaw and soil temperature data

In this study, we utilized two datasets from the SMAP mission. First, the Enhanced Level-3 (L3) Freeze/Thaw product (SPL3FTP_E) provides daily soil freeze-thaw state classifications using radar backscatter measurements at a 9 km spatial resolution, from the SMAP radiometer (1.41 GHz) during the 6:00 descending and 18:00 ascending half-orbit passes[62]. We used the variables 'freeze_thaw' and 'freeze_thaw_time_utc' to assess freeze-thaw states and ensure temporal consistency. Second, the Level-4 product (SPL4SMAU) provides 3-hourly surface temperature, soil temperature (0–5 cm), and soil moisture (0–5 cm) globally, maintaining the same spatial resolution as the freeze-thaw product[63]. The dataset spans from July 1, 2015, to June 30, 2022, with rigorous quality control to ensure reliability over the 7-year monitoring period.

Previous studies have demonstrated that SMAP's freeze-thaw products outperform other microwave-based products in terms of both statistical performance and spatial-temporal patterns[35,36]. However, the SPL3FTP_E and SPL4SMAU products differ in their temporal standards: freeze-thaw data is based on local solar time (6:00 and 18:00), while soil moisture data follows UTC. To align these datasets, we converted UTC times to local solar times using a 15°/hour factor and adjusted the timing using the 'freeze_thaw_time_utc' variable, ensuring a maximum time difference of 1 hour. This alignment is critical for accurate event detection and analysis of freeze-thaw dynamics and soil temperature variability.

The original 3-hourly soil temperature data were resampled to hourly intervals after converting to local solar time using nearest-neighbour interpolation. Specifically, each 3-hourly record was replicated to the corresponding three consecutive hourly time steps, assuming that the temperature remained constant within each 3-hour interval. This simple replication method was adopted instead of higher-order temporal interpolation (e.g., linear or spline interpolation) to avoid distorting the inherent correspondence between temperature and soil freeze–thaw states, which are fixed during each time step but could be artificially perturbed by interpolation.

## Definition of freeze-thaw events

Sub-zero Unfrozen State (SUS) events are defined in this study as instances where soil temperatures fall below 0°C, while freeze-thaw monitoring reveals an unfrozen soil condition. Conversely, instances where the soil temperature exceeds 0°C but the state indicates freezing are defined as Above-zero Frozen State (AFS) events. To ensure continuous records of freeze-thaw process without disruption by the calendar year, this study defines the annual cycle as beginning on July 1 of each year and ending on June 30 of the following year. Furthermore, to ensure the robustness of our findings, SUS events were analyzed individually for each year before calculating the multi-year average characteristics, effectively capturing the long-term trends while accounting for interannual variability.

Based on the phase change characteristics observed within ± 12 hours relative to the event occurrence (transitions of freeze-thaw states before, at, and following each SUS event), SUS events were classified into four types: Consistent Thawing (CT: Thawed → Thawed → Thawed), Thawing Process (TP: Frozen→Thawed→Thawed), Freezing Process (FP: Thawed → Thawed → Frozen), and Diel Freeze-Thaw alternations (DFT: Frozen → Thawed → Frozen).

We adopted a monthly temporal framework to statistically analyze distinctions in SUS event typologies during freeze-thaw cycles, effectively mitigating biases from seasonal soil biogeochemical variations. It is well established that the freezing point of bound water in soils is substantially lower than that of free water[44,64], with lower water content nonlinearly intensifying the freezing point depression of soil[44,65,66]. Therefore, we use a soil moisture threshold greater than the permanent wilting point (PWP) to exclude super dry soils and focus on the roles of salinity and other soil properties in modulating the freezing point depression of free water.

# Feature Selection

To identify SUS events, we constructed a comprehensive netCDF dataset comprising 137,554 grid points. This dataset integrated three distinct categories of variables: (1) geographical parameters, including longitude (Lon), latitude (Lat), and event timing (UTC/Solar); (2) intrinsic soil properties, such as permanent wilting point (PWP), soil organic carbon (SOC), cation exchange capacity (CEC), and particle composition (Sand, Clay, Silt); and (3) thermal-hydrological dynamics, encompassing soil temperature, surface temperature, soil moisture content, and freeze-thaw states. The superior temporal resolution of the three dynamic datasets relative to freeze-thaw state records enabled systematic capture of freeze-thaw state transitions surrounding SUS events, alongside concurrent surface temperature, soil temperature, and moisture fluctuations. These dynamic variables facilitated the derivation of four thermal variation metrics: Soil-Surface Temperature Difference (SSTD), Hours Below 0°C (HB0C), Soil Temperature Time Derivative (STTD), and Soil Temperature Change Rates at 1/6/12-hour intervals (ST1/6/12CR).

To characterize the seasonal signatures of SUS events, we implemented cyclical month encoding using paired sine (M_sin) and cosine (M_cos) transformations. The sinusoidal component captures the symmetrical annual periodicity, while the cosine term resolves phase-specific extrema. The orthogonal

combination of these terms uniquely maps calendric months, providing a parametric representation that explicitly incorporates cyclic priors into regression frameworks. This approach effectively constrains the model search space, enhancing the ability to identify seasonally dependent patterns in SUS events.

$$\theta = \frac{2\pi}{12}(n-1) \quad (1)$$

$$\mathrm{M_sin} = \sin(\theta) \quad (2)$$

$$\mathrm{M_cos} = \cos(\theta) \quad (3)$$

# XGBoost framework

XGBoost is a machine learning algorithm developed based on the gradient boosting framework of decision tree learning algorithms, and it is recognized for its outstanding efficiency in handling classification tasks[67]. Compared to algorithms like random forests, XGBoost offers superior prediction and classification accuracy, lower risk of overfitting and higher computational efficiency. For the classification task distinguishing between SUS and frozen events under 0°C, we generated a dataset comprising twice the number of grid points through spatial averaging of all SUS and frozen event parameters per grid cell. The model was configured with binary logistic regression as the objective function, utilizing instantaneous freeze-thaw states (coded 0: thawed, 1: frozen) as target variables and the selected environmental covariates as predictors. For the regression task aiming to predict the occurrence temperature during SUS events (freezing-point depression effects), we expanded the sample size by a factor of 12 using monthly averaged SUS event temperatures per grid cell. Temperature values when SUS events occur served as continuous target variables.

Both models incorporate optimized hyperparameters including ‘max_depth’ (tree complexity), ‘learning_rate’ (shrinkage factor), ‘subsample’ (stochastic instance sampling), ‘colsample_bytree’ (feature subspace sampling), ‘n_estimators’ (boosting iterations), ‘gamma’ (regularization penalty), and ‘min_child_weight’ (leaf node constraints). We implemented 5-fold cross-validation to rigorously evaluate model performance, partitioning the dataset into five stratified subsets. For each iteration, four subsets trained the model, while the remaining fold served as the validation set. This process repeated until all folds functioned as validation data, ensuring comprehensive data utilization while maintaining independence between training and validation phases.

For the freeze-thaw state classification model, performance metrics including accuracy, precision, recall, and the area under the receiver operating characteristic curve (AUC-ROC) are computed to evaluate classification efficacy. For the SUS event temperature prediction model, model performance was rigorously assessed using mean squared error (MSE), mean absolute error (MAE), and the coefficient of determination ($R^2$).

# Interpretation Methods

Interpretable machine learning methods like the SHAP (Shapley Additive exPlanations) method, based on cooperative game theory[68], can visualize the contribution of each feature to model predictions. We calculated global feature importance by averaging the absolute SHAP values across all samples[69]. A SHAP value quantifies the contribution of each feature to the prediction for a given sample[70]. For the i-th sample with k features, the predicted value can be expressed as:

$$y_i = y_{base} + f(x_{i,1}) + f(x_{i,2}) + \cdots + f(x_{i,k})$$

4

where $y_{base}$ is the baseline of the entire model (usually the mean of the target variable of all samples) and $f(x_{i,j})$ is the SHAP value of each feature variable ($x_{i,j}$, the value of the j-th feature for the i-th sample). A positive $f(x_{i,j})$ indicates the feature increases the prediction above the baseline, while a negative value indicates the feature has negative contribution to the prediction. This additive property ensures the sum of all feature contributions equals the model's prediction for each sample. In this study, we used the Python package "shap" to integrate with the XGBoost model for calculating and visualizing SHAP values.

**Determination of $T_f$ and $T_{sc}$ using SMAP**

To capture the supercooling–latent heat release process, we focus on 12-hour soil temperature sequences associated with thawing-to-freezing transitions. We first exclude all sequences in which soil temperature remains entirely above 273.15 K throughout the 12-hour window, as such records do not contain physically relevant freezing signals. In addition, records during the thawing state with soil moisture below the wilting point are excluded to ensure the presence of liquid water available for phase change. We calculated the two inflection points of the resampled hourly (original 3-hourly) soil temperature curve and retain only those sequences where the local minimum precedes the local maximum, indicating a rapid warming caused by latent heat release following supercooling (see schematic in Supplementary Fig. 1). This approach allows for the extraction of key metrics—the minimum supercooling temperature ($T_{sc}$) and the freezing equilibrium temperature or freezing point ($T_f$) —for each freezing event at each grid cell.

**Determination of $T_f$ and $T_{sc}$ using in-situ observations**

To validate above satellite-derived $T_f$ values, we compared them with in-situ estimates derived from half-hourly observations of soil temperature (TS_F_MDS_x), soil heat flux (G_F_MDS) and volumetric liquid water content (SWC_F_MDS_x) at three soil depths from FLUXNET eddy covariance flux tower sites spanning 2013–2024[71,72]. Flux tower sites were first screened for data availability and sufficiency of the three variables at least for the top soil layer (0–5 cm); 33 sites provided enough observations to calculate site-level $T_f$ using the multi-criteria hydrothermal diagnostic framework described below. To

enable direct spatial validation against SMAP, each qualifying site was paired with its corresponding SMAP pixel, and $T_f$ for each pixel was retrieved using the remote sensing method described in the preceding section. Because SMAP observations have substantially coarser temporal resolution than flux tower records, $T_f$ retrieval at the pixel level is inherently more challenging; pixels for which no reliable $T_f$ could be identified were excluded from the comparison. This filtering yielded 19 matched site-pixel pairs, comprising the following flux tower sites: US-xCP, US-CS6, US-xNG, US-xMB, US-DFC, CA-ARF, FI-Var, US-xBL, CA-TP1, US-xYE, US-NR1, US-Oho, US-Syv, US-GLE, CA-Cbo, US-xWD, US-xUK, US-xAB, and US-Prr, whose locations are shown in Fig. 4c.

Soil freezing is considered a continuous process, and our analysis focused on physically critical observational segments when both supercooling and freezing equilibrium states can be identified. Given that FLUXNET datasets lack explicit soil freeze/thaw state classification, we implemented a multi-criteria diagnostic framework to identify freezing events and determine the associated values of $T_f$ and $T_{sc}$. This framework integrates the coupled signals of energy flux and soil hydrothermal dynamics. The three requisite soil hydrothermal variables TS_F_MDS_x, G_F_MDS and SWC_F_MDS_x were obtained from the FLUXNET FULLSET product, which reports gap-filled soil temperature and volumetric liquid water content time series for multiple soil layers from upper 5-cm to approximately 50-cm depth. These layered datasets provide relative depth indices across sites, but the exact physical sensor depths are site-specific and are not retained in the FULLSET product. To ensure that freezing-related analyses are representative of specific, consistent soil-layer conditions, we further examined site-level sensor metadata using the Measurement Height data from AmeriFlux BASE data products, which reports sensor height/depth and instrument information provided by site teams or historical records. Based on these metadata, TS/SWC_F_MDS_1 and TS/SWC_F_MDS_2 soil temperature records were found to most consistently correspond to the two shallowest measurement depths across sites. Accordingly, for each site we selected either TS/SWC_F_MDS_1 or TS/SWC _F_MDS_2 such that the soil temperature time series best represents near-surface conditions for the upper ~ 5 cm of the soil profile, although small variation exists in the physical depth across sites. Following a similar procedure, concurrent soil temperature, soil heat flux, and volumetric liquid water content data for two representative deeper layers (~ 20 and ~ 50 cm) were collected across sites (the number of sites with available data decreases with measurement depth). The final selected data was primarily from the 2013–2024 period.

Based on the curated dataset, candidate freezing events were initially identified by aligning soil temperature trajectories with the characteristic evolution pattern (schematic in Supplementary Fig. 1). These candidates were further refined by requiring a synchronous decline in volumetric soil water content and a soil heat flux signature indicative of latent heat release. Specifically, freezing-event data records were constructed by requiring temporal continuity of observed soil temperature and a negative soil heat flux (indicating heat loss to the atmosphere) at a 30-min resolution with a minimum duration of 3 hours, consistent with the temporal sampling of SMAP satellite-based freeze–thaw products. Within each continuous freezing event, we extracted the temperature-increasing segment and mandated it be bounded by temperature decreases both before and after the segment. Critically, this thermal evolution

must be synchronized with a reduction in soil volumetric water content between the two turning points, signifying the phase transition from liquid water to ice. As a result, only events exhibiting a characteristic soil temperature trajectory—initial cooling, followed by transient latent-heat-driven warming, and subsequent cooling—coupled with consistent water depletion were retained. This evolution represents the typical soil freezing curve, where latent heat release temporarily buffers cooling while liquid water is concurrently consumed. Events lacking this two-turning-point temperature pattern, exhibiting a state of soil heat absorption from the atmosphere, or showing an increase in soil volumetric water were excluded from subsequent analyses.

The joint occurrence of sub-zero soil temperature[17,19] and an energy signal consistent with latent heat release, complemented by a concurrent reduction in soil volumetric water content and the characteristic soil temperature evolution, provides a conservative and physically consistent diagnosis of active soil freezing processes across heterogeneous sites. Following this approach, freezing events and the associated values of $T_f$ and $T_{sc}$ were determined for each site in the data collection.

## Declarations

# Data Availability

The soil freeze-thaw states (twice daily) and soil moisture data (3-hourly) are two of the SMAP baseline science data products, sourced from the National Snow and Ice Data Center. The product numbers are SPL3FTP_E and SPL4SMAU, respectively. These can be accessed at the following URLs: https://nsidc.org/data/spl3ftp_e/versions/4 and https://nsidc.org/data/spl4smau/versions/7. The data on soil morphology, chemical, and physical properties are sourced from SoilGrids, available at International Soil Reference and Information Centre (ISRIC)'s SoilGrids system: https://www.isric.org/explore/soilgrids/faq-soilgrids-2017. The in-situ eddy covariance flux observations utilized in this study were sourced from the AmeriFlux FLUXNET data product and the ICOS Warm Winter 2020 release. These datasets are publicly available through the AmeriFlux repository (https://ameriflux.lbl.gov/) and the ICOS Carbon Portal (https://doi.org/10.18160/2G60-ZHAK), respectively.

# Code Availability

The maps and statistical figures are created using Python scripts. The code and data necessary to reproduce the results presented in this study have been deposited to Zenodo: https://doi.org/10.5281/zenodo.19887110. The detailed code for generating all intermediate datasets will be publicly released before publication.

# Competing Interest Statement:

The authors declare no competing interests.

# Author Contributions:

Y.F. carried out funding acquisition and supervision. Y.F. and Z.D. conceived the study. Z.D. collected data and performed analyses. Z.D. and Y.F. wrote the manuscript.

# Acknowledgments

The authors acknowledge supports from Guangdong Basic and Applied Basic Research Foundation (grant no. 2025A1515510023), Shenzhen Science and Technology Program (grant no. ZDSYS20220606100806014) and Scientific Research Start-up Funds from Tsinghua Shenzhen International Graduate School (grant no. QD2023021C).

## References

1. Kurylyk, B. L. & Watanabe, K. The mathematical representation of freezing and thawing processes in variably-saturated, non-deformable soils. *Adv. Water Resour*. 60, 160–177 (2013).
2. Meredith, M. et al. Polar Regions. In: IPCC Special Report on the Ocean and Cryosphere in a Changing Climate. Cambridge University Press, Cambridge, UK and New York, NY, USA, pp. 203–320 (2019).
3. Mu, C. et al. The status and stability of permafrost carbon on the Tibetan Plateau. *Earth Sci. Rev.* 211, 103433 (2020).
4. Box, J. E. et al. Key indicators of Arctic climate change: 1971–2017. *Environ. Res. Lett.* 14, 045010 (2019).
5. Landrum, L. & Holland, M. M. Extremes become routine in an emerging new Arctic. *Nat. Clim. Change* 10, 1108–1115 (2020).
6. Schuur, E. A. G. et al. Climate change and the permafrost carbon feedback. *Nature* 520, 171–179 (2015).
7. Natali, S. M. et al. Large loss of CO2 in winter observed across the northern permafrost region. *Nat. Clim. Change* 9, 852–857 (2019).
8. Smith, S. L., O'Neill, H. B., Isaksen, K., Noetzli, J. & Romanovsky, V. E. The changing thermal state of permafrost. *Nat. Rev. Earth Environ*. 3, 10–23 (2022).
9. Wang, H., Vanapalli, S. K. & Li, X. A unified model for the soil freezing characteristic curve based on pore size distribution and principles of thermodynamics. *Water Resour. Res*. 61, e2024WR038715 (2025).
10. Tian, H., Wei, C., Wei, H. & Zhou, J. Freezing and thawing characteristics of frozen soils: bound water content and hysteresis phenomenon. *Cold Reg. Sci. Technol*. 103, 74–81 (2014).
11. Wei, X., Shen, Y., Wei, Z., Wang, Y. & Wang, Y. Resistivity and unfrozen water content of moraine soil at freezing temperatures: experiments and thermodynamic modeling. *Cold Reg. Sci. Technol.* 235,

104494 (2025).
12. Feng, S. et al. Miscellaneous methods for determination of unfrozen water content in frozen soils. *J. Hydrol.* 631, 130802 (2024).
13. Wang, C. et al. Quantification of chloride saline soil freezing–thawing temperature threshold based on thermodynamic theory. *Acta Geotech*. 20, 1049–1068 (2025).
14. Devoie, É. G., Gruber, S. & McKenzie, J. M. A repository of measured soil freezing characteristic curves: 1921 to 2021. *Earth Syst. Sci. Data* 14, 3365–3377 (2022).
15. Lamas, C. P., Vega, C. & Noya, E. G. Freezing point depression of salt aqueous solutions using the Madrid-2019 model. *J. Chem. Phys.* 156, 134503 (2022).
16. Zhou, J., Wei, C., Lai, Y., Wei, H. & Tian, H. Application of the generalized Clapeyron equation to freezing point depression and unfrozen water content. *Water Resour. Res*. 54, 9412–9431 (2018).
17. Huang, X. & Rudolph, D. L. Numerical study of coupled water and vapor flow, heat transfer, and solute transport in variably-saturated deformable soil during freeze–thaw cycles. *Water Resour. Res*. 59, e2022WR032146 (2023).
18. Zhang, J. et al. Numerical study on the hydro-thermal-chemical–mechanical coupling mechanism in sulfate saline soil under freeze–thaw cycles. *Comput. Geotech*. 176, 106803 (2024).
19. Li, K. et al. Study of supercooling phenomena in soil-water systems based on nucleation theory: quantifying supercooling duration. *Cold Reg. Sci. Technol.* 242, 104753 (2026).
20. Chen, C. et al. Comprehensive assessment of seasonally frozen ground changes in the Northern Hemisphere based on observations. *J. Geophys. Res. Atmos*. 127, e2022JD037306 (2022).
21. Guo, D., Yang, M. & Wang, H. Characteristics of land surface heat and water exchange under different soil freeze/thaw conditions over the central Tibetan Plateau. *Hydrol. Process*. 25, 2531–2541 (2011).
22. Zhang, Z. et al. Degraded frozen soil and reduced frost heave in China due to climate warming. *Sci. Total Environ*. 893, 164914 (2023).
23. Lawrence, D. M. et al. The Community Land Model version 5: description of new features, benchmarking, and impact of forcing uncertainty. *J. Adv. Model. Earth Syst*. 11, 4245–4287 (2019).
24. Zhu, M. et al. An analytical model of active layer depth under changing ground heat flux. *J. Geophys. Res. Atmos*. 129, e2023JD039453 (2024).
25. Peng, X. et al. Active layer thickness and permafrost area projections for the 21st century. *Earth's Future* 11, e2023EF003573 (2023).
26. Niu, G.-Y. & Yang, Z.-L. Effects of frozen soil on snowmelt runoff and soil water storage at a continental scale. *J. Hydrometeorol*. 7, 937–952 (2006).
27. Koven, C. D., Riley, W. J. & Stern, A. Analysis of permafrost thermal dynamics and response to climate change in the CMIP5 Earth system models. *J. Clim*. 26, 1877–1900 (2013).
28. Yang, K., Wang, C. & Li, S. Improved simulation of frozen-thawing process in land surface model (CLM4.5). *J. Geophys. Res. Atmos.* 123, 13,238–13,258 (2018).

29. Li, Q., Xue, Y. & Liu, Y. Impact of frozen soil processes on soil thermal characteristics at seasonal to decadal scales over the Tibetan Plateau and North China. *Hydrol. Earth Syst. Sci.* 25, 2089–2107 (2021).
30. Wu, M. et al. Improved soil hydrological modeling with the implementation of salt-induced freezing point depression in CoupModel: model calibration and validation. *J. Hydrol.* 596, 125693 (2021).
31. Guimond, J. A., Mohammed, A. A., Walvoord, M. A., Bense, V. F. & Kurylyk, B. L. Saltwater intrusion intensifies coastal permafrost thaw. *Geophys. Res. Lett*. 48, e2021GL094776 (2021).
32. Nitzbon, J. et al. No respite from permafrost-thaw impacts in the absence of a global tipping point. *Nat. Clim. Change* 14, 573–585 (2024).
33. He, H. et al. Critical review of the models used to determine soil water content using TDR-measured apparent permittivity. *Adv. Agron.* 182, 169–219 (2023).
34. Zhou, X., Zhou, J., Kinzelbach, W. & Stauffer, F. Simultaneous measurement of unfrozen water content and ice content in frozen soil using gamma ray attenuation and TDR. *Water Resour. Res.* 50, 9630–9655 (2014).
35. Chen, Y. et al. Evaluation of SMAP, SMOS, and AMSR2 soil moisture retrievals against observations from two networks on the Tibetan Plateau. *J. Geophys. Res. Atmos*. 122, 5780–5792 (2017).
36. Zheng, J. et al. Use of a new Tibetan Plateau network for permafrost to characterize satellite-based products errors: an application to soil moisture and freeze/thaw. *Remote Sens. Environ.* 300, 113899 (2024).
37. Du, Y., Wang, Z., Jiang, L., Calzavarini, E. & Sun, C. Sea water freezing modes in a natural convection system. *J. Fluid Mech*. 960, A35 (2023).
38. Shah, R. & Mir, B. A. The freezing point of soils and the factors affecting its depression. in Advances in Construction Management (eds Loon, L. Y., Subramaniyan, M. & Gunasekaran, K.) 157–166 https://doi.org/10.1007/978-981-16-5839-6_14 (Springer, 2022).
39. Hu, S., Zhang, C. & Lu, N. Quantifying coupling effects between soil matric potential and osmotic potential. *Water Resour. Res.* 59, e2022WR033779 (2023).
40. Kozlowski, T. Some factors affecting supercooling and the equilibrium freezing point in soil–water systems. *Cold Reg. Sci. Technol.* 59, 25–33 (2009).
41. Wang, C. et al. Study on the supercooling characteristics of freezing soil based on nucleation theory. *Water Resour. Res*. 59, e2023WR034800 (2023).
42. Hong, J. et al. Imaging surface structure and premelting of ice Ih with atomic resolution. *Nature* 630, 375–380 (2024).
43. Wang, S., Wang, Q., Xu, J. & Ding, J. Effect of freeze-thaw on freezing point and thermal conductivity of loess. *Arab. J. Geosci.* 13, 206 (2020).
44. Zhou, J., Meng, X., Wei, C. & Pei, W. Unified soil freezing characteristic for variably-saturated saline soils. *Water Resour. Res*. 56, e2019WR026648 (2020).

45. Kleidon, A. Thermodynamic Foundations of the Earth System https://doi.org/10.1017/CBO9781139342742 (Cambridge Univ. Press, 2016).
46. Amankwah, S. K., Ireson, A. M., Maulé, C., Brannen, R. & Mathias, S. A. A model for the soil freezing characteristic curve that represents the dominant role of salt exclusion. *Water Resour. Res*. 57, e2021WR030070 (2021).
47. Zhang, M., Zhang, X., Lai, Y., Lu, J. & Wang, C. Variations of the temperatures and volumetric unfrozen water contents of fine-grained soils during a freezing–thawing process. *Acta Geotech*. 15, 595–601 (2020).
48. Shafique, U. et al. Chemistry of ice: migration of ions and gases by directional freezing of water. *Arab. J. Chem.* 9, S47–S53 (2016).
49. Wu, Y., Tang, A.-M., Pereira, J.-M., Sidi-Boulenouar, R. & Hu, L. Effect of water salinity on the soil freezing-thawing characteristic curve of sandy soils. *J. Hydrol.* 672, 135359 (2026).
50. Wang, M. et al. Chemical characteristics of salt migration in frozen soils during the freezing-thawing period. *J. Hydrol.* 606, 127403 (2022).
51. Hansen, J. E. et al. Global warming has accelerated: are the United Nations and the public well-informed? *Environment* 67, 6–44 (2025).
52. IPCC, *Climate Change 2021 – The Physical Science Basis: Working Group I Contribution to the Sixth Assessment Report of the Intergovernmental Panel on Climate Change*. (Cambridge University Press, Cambridge, 2023).
53. Armstrong McKay, D. I. et al. Exceeding 1.5°C global warming could trigger multiple climate tipping points. *Science* 377, eabn7950 (2022).
54. Stroeve, J. C. et al. Disappearing landscapes: the Arctic at + 2.7°C global warming. *Science* 387, 616–621 (2025).
55. Li, J. et al. Amplified Arctic–boreal fire regimes from permafrost thaw feedbacks. *Nat. Geosci*. 19, 279–290 (2026).
56. Chai, L. et al. QLB-NET: a dense soil moisture and freeze–thaw monitoring network in the Qinghai Lake Basin on the Qinghai–Tibetan Plateau. *Bull. Am. Meteorol. Soc.* 105, E584–E604 (2024).
57. Pan, Z. & Duan, A. Influence of the Tibetan Plateau on the coupling of the North Pacific–North Atlantic pressure systems. *Atmos. Res.* 295, 107026 (2023).
58. Tang, S. et al. Resonance between projected Tibetan Plateau surface darkening and Arctic climate change. *Sci. Bull*. 69, 367–374 (2024).
59. Hua, H. et al. Accelerated land surface greening caused by earlier permafrost thawing. *Nat. Commun.* 17, 920 (2026).
60. Hengl, T. et al. SoilGrids250m: global gridded soil information based on machine learning. *PLoS ONE* 12, e0169748 (2017).
61. Batjes, N. H., Calisto, L. & de Sousa, L. M. Providing quality-assessed and standardised soil data to support global mapping and modelling (WoSIS snapshot 2023). *Earth Syst. Sci. Data* 16, 4735–4765

(2024).
62. Xu, X. et al. SMAP Enhanced L3 Radiometer Global and Northern Hemisphere Daily 9 km EASE-Grid Freeze/Thaw State (SPL3FTP_E, Version 4). NASA National Snow and Ice Data Center Distributed Active Archive Center https://doi.org/10.5067/NQLCDOZJYAKX (2023).
63. Reichle, R. et al. SMAP L4 Global 3-hourly 9 km EASE-Grid Surface and Root Zone Soil Moisture Analysis Update (SPL4SMAU, Version 7). NASA National Snow and Ice Data Center Distributed Active Archive Center https://doi.org/10.5067/LWJ6TF5SZRG3 (2022).
64. Bing, H. & Ma, W. Laboratory investigation of the freezing point of saline soil. *Cold Reg. Sci. Technol*. 67, 79–88 (2011).
65. Kozlowski, T. A simple method of obtaining the soil freezing point depression, the unfrozen water content and the pore size distribution curves from the DSC peak maximum temperature. *Cold Reg. Sci. Technol*. 122, 18–25 (2016).
66. Low, P. F., Anderson, D. M. & Hoekstra, P. Some thermodynamic relationships for soils at or below the freezing point: 1. Freezing point depression and heat capacity. *Water Resour. Res*. 4, 379–394 (1968).
67. Lu, H. & Ma, X. Hybrid decision tree-based machine learning models for short-term water quality prediction. *Chemosphere* 249, 126169 (2020).
68. Lundberg, S. M. & Lee, S. I. A unified approach to interpreting model predictions. In Proceedings of the 31st International Conference on Neural Information Processing Systems (NIPS'17). Curran Associates Inc., Red Hook, NY, USA, 4768–4777 (2017).
69. Molnar, C., Casalicchio, G. & Bischl, B. Quantifying Model Complexity via Functional Decomposition for Better Post-hoc Interpretability. In: Cellier, P., Driessens, K. (eds) Machine Learning and Knowledge Discovery in Databases. ECML PKDD 2019. Communications in Computer and Information Science, vol 1167. Springer, Cham (2020).
70. Rodríguez-Pérez, R. & Bajorath, J. Interpretation of machine learning models using Shapley values: application to compound potency and multi-target activity predictions. J. Comput. *Aided Mol. Des*. 34, 1013–1026 (2020).
71. Chu, H. et al. AmeriFlux BASE data pipeline to support network growth and data sharing. *Sci. Data* 10, 614 (2023).
72. Warm Winter 2020 Team & ICOS Ecosystem Thematic Centre. Warm Winter 2020 ecosystem eddy covariance flux product for 73 stations in FLUXNET-Archive format—release 2022-1 (Version 1.0). *ICOS Carbon Portal* https://doi.org/10.18160/2G60-ZHAK (2022).

# Figures

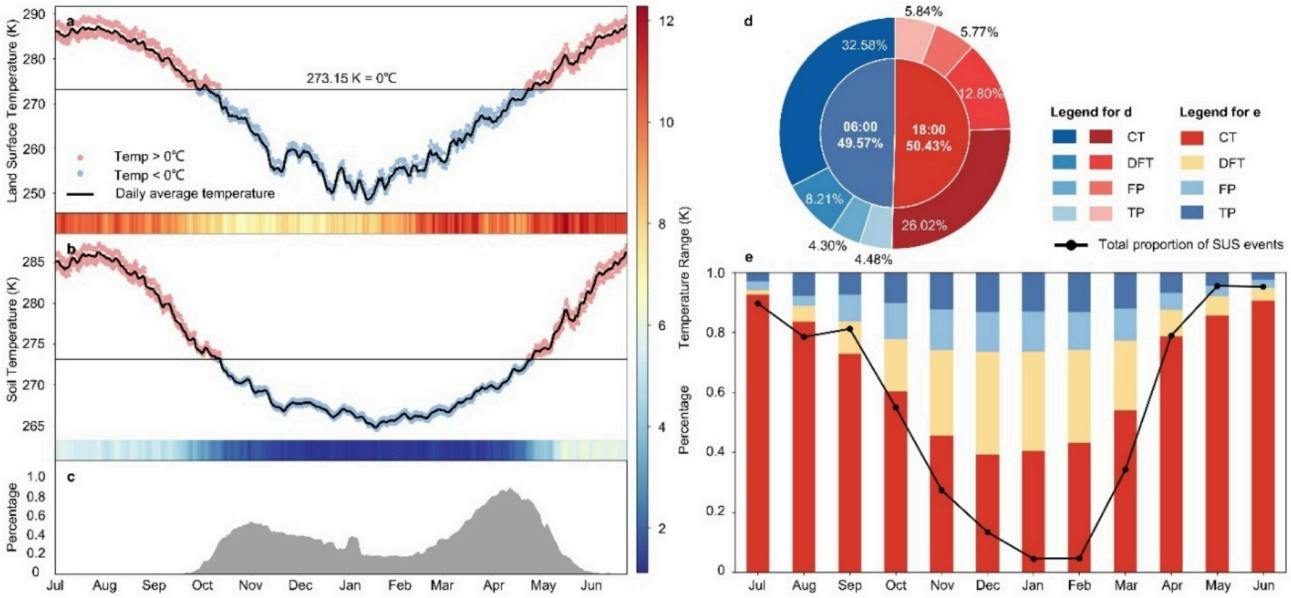
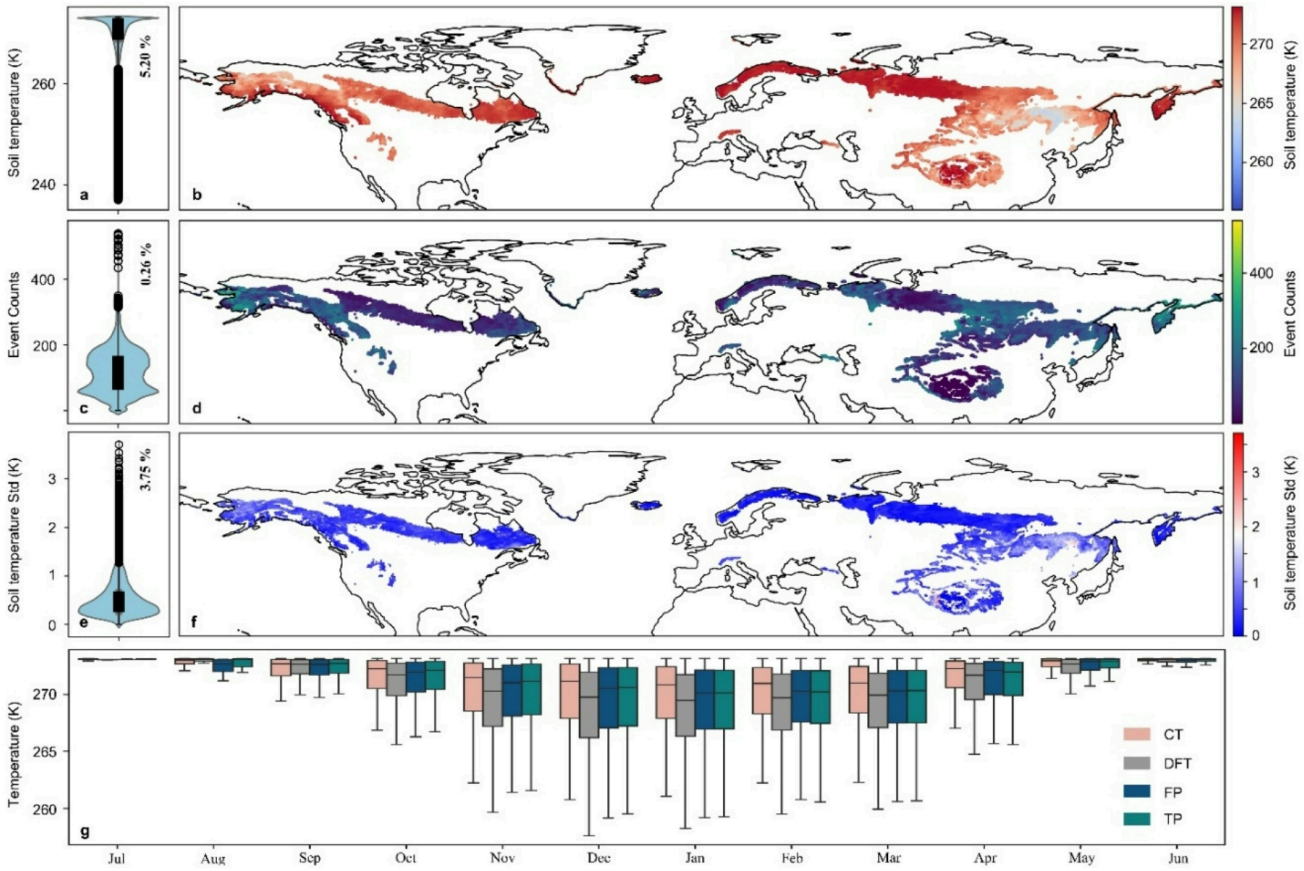


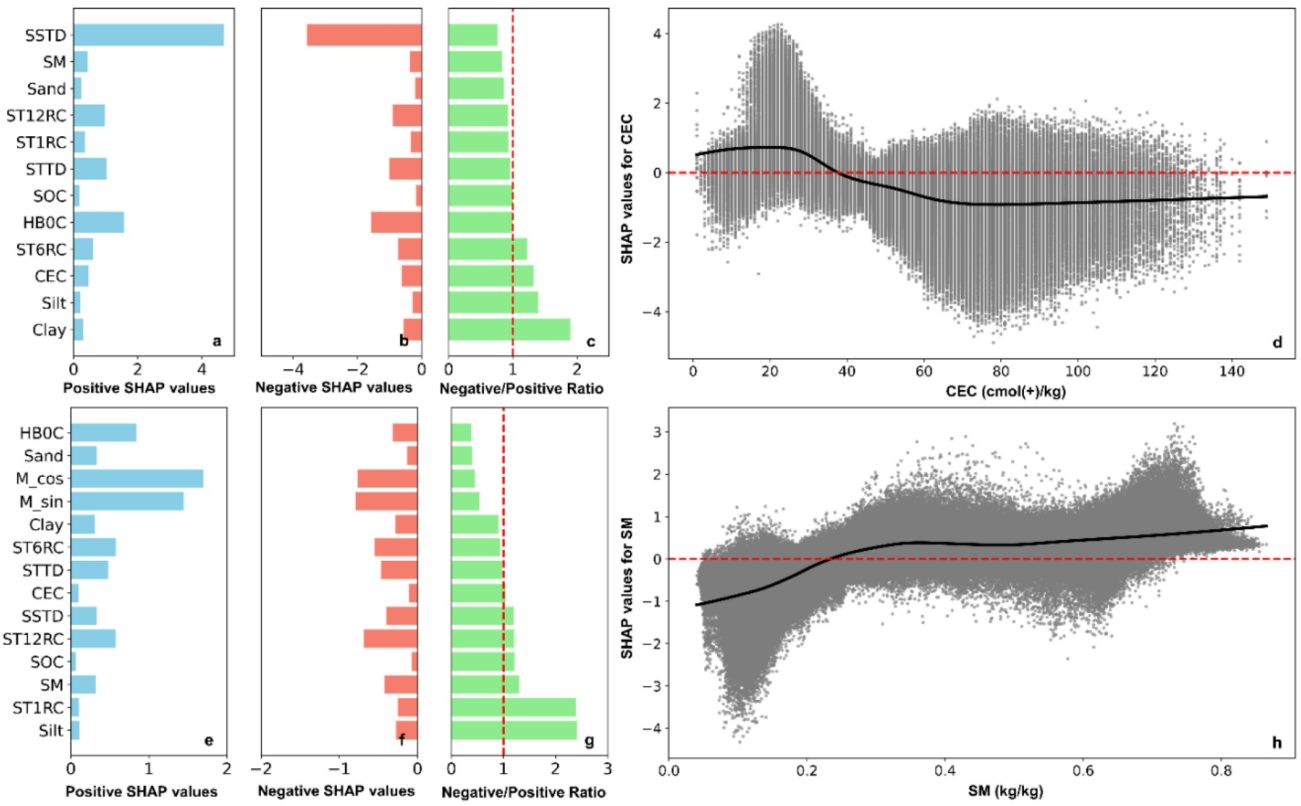

**Figure 1**

**Seasonal characteristics of SUS events using SMAP soil temperature and freeze–thaw state data.** (a) Annual distribution of hourly land surface temperatures and their daily averages. The solid black line represents the daily average of the land surface temperature, and the red and blue scattered points represent hourly records greater than 0 and less than 0, respectively. The color band below the scatter plot represents the difference between the maximum and minimum values of the day. (b) Annual distribution of hourly temperatures and their daily averages. The solid black line represents the daily average of the soil temperature, and the red and blue scattered points represent hourly records greater than 0 and less than 0, respectively. The color band below the scatter plot represents the difference between the maximum and minimum values of the day. (c) The multi-year average daily distribution of SUS event frequency, expressed as a fraction of the annual total SUS frequency (see Supplementary Table 1 for monthly statistics of all SUS events). (d) Proportions of four categories of SUS events according to their occurrence time during 2015-2022. Blue for events occurring in the morning (06:00) and red for events occurring in the evening (18:00). (e) Proportions of four categories of SUS events during each month (color bars). The black line and dots indicate the overall proportion of SUS events relative to all soil temperature conditions below 0 °C (including both frozen and unfrozen states).



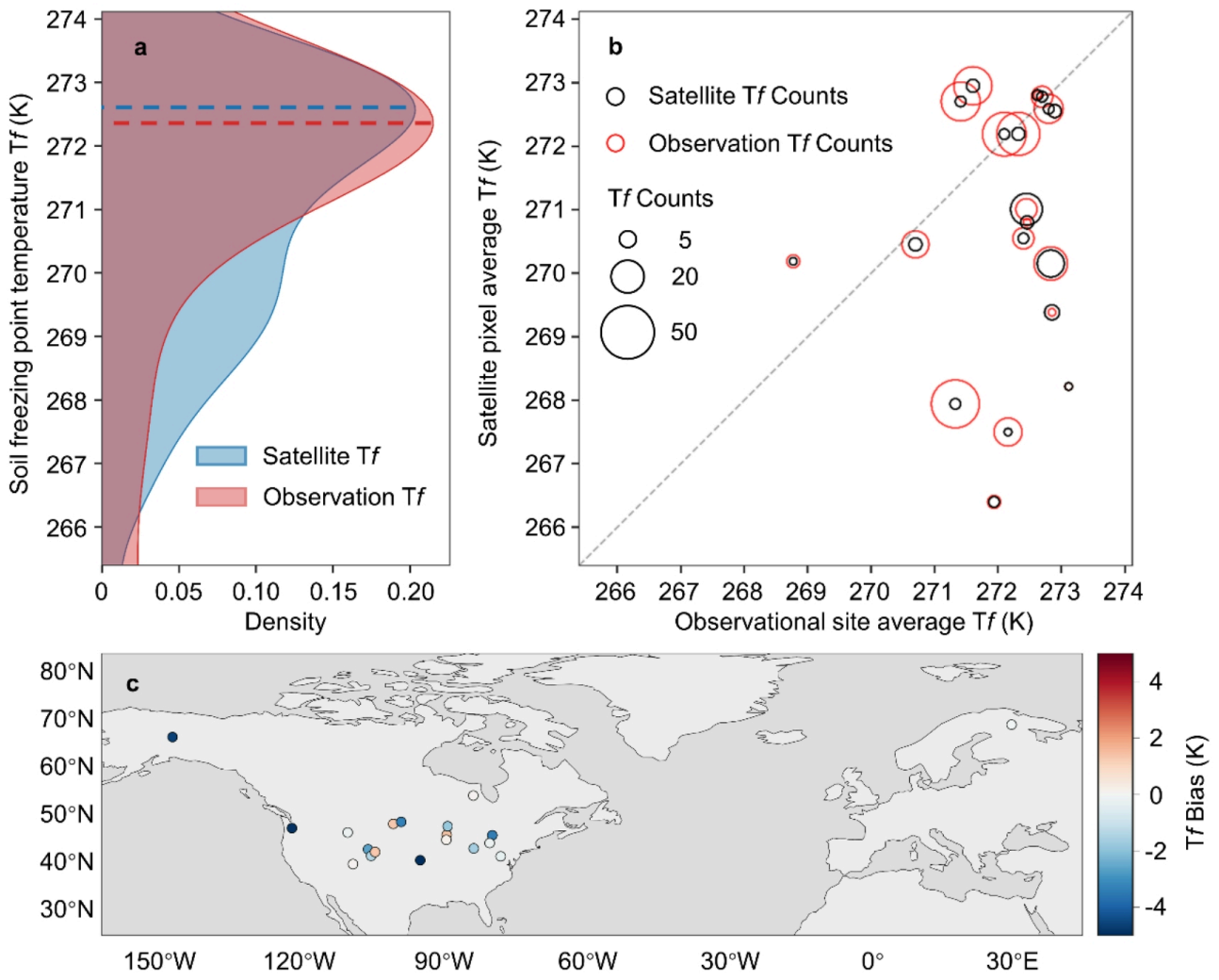

## Figure 2

**Spatial distribution and seasonal characteristics of temperature during SUS events.** (a) The violin plot shows the average soil temperature distribution of SUS events, and the values on the violin plot represent the proportion of values outside the confidence interval. Temperature values are considered outliers if they lay outside the range Q1−1.5×IQR, Q3+1.5×IQR, where Q1 and Q3 denote the 25th and 75th percentiles and their difference is IQR. (b) Spatial distribution of soil temperatures during SUS events. (c) Violin plot of the occurrence of SUS events. (d) Spatial distribution of SUS event occurrences. (e) Violin plot of the standard deviation of soil temperatures during SUS events. (f) Spatial distribution of the standard deviation of soil temperatures during SUS events. (g) Box plot of occurrence soil temperatures for different types of SUS events across the Northern Hemisphere during each month.




## Figure 3

**Quantification of multi-feature contributions in all SUS events.** (a-c) Positive SHAP values, negative SHAP values and the absolute SHAP ratios of (b) divided by (a), respectively, of different features in the XGBoost classification model. Negative SHAP values in (b) and absolute SHAP ratios > 1 in (c) indicate net contributions of features that promote occurrences of SUS events. (d) Scatterplot of CEC feature SHAP values (The black line represents a LOWESS-smoothed curve (frac = 1/3, it = 0), highlighting the general trend in the SHAP value distribution.) (e-g) Same as in (a-c) but for the regression model. Here negative SHAP values in (f) and absolute SHAP ratios > 1 in (g) indicate freezing-point depression effects of respective features during SUS events. (h) SM feature SHAP values scatter plot. Variable abbreviations are defined as follows: SSTD: Soil–Surface Temperature Differential, HB0C: Hours Below 0 °C, STTD: Soil Temperature Time Derivative, ST1RC / ST6RC / ST12RC: Soil Temperature Change Rate at 1 / 6 / 12 hours, SM: Soil Moisture, CEC: Cation Exchange Capacity, SOC: Soil Organic Carbon, Clay / Silt / Sand: Soil particle composition, M_sin / M_cos: Sine and Cosine transformations of calendar month.




## Figure 4

**Comparison of freezing points derived from satellite and in-situ observations.** (a) Distribution of soil freezing points from 19 collocated SMAP pixels and FLUXNET sites (see Methods section "Determination of $T_f$ and $T_{sc}$ using in-situ observations" for details). The KDE peaks of temperature distribution of soil freezing events at flux tower sites and SMAP pixels are 272.37 K and 272.57 K, respectively. The data samples derived from SMAP and in-situ observations exhibit no significant differences both in distributional characteristics (K-S test: $p$ = 0.0648) and in mean values (Welch's $t$-test: $p$ = 0.0522). (b) Scatter plots of $T_f$ temperature distribution and freezing event counts for the 19 collocated site-pixel pairs. The black and red circles represent whether the soil freezing point was derived from satellite data or from in-situ observations. The size of the circles indicates the number of $T_f$ values. The FLUXNET sites often have more $T_f$ values derived due to finer temporal resolution of in-situ

observations. (c) Difference between temporally averaged $T_f$ at each SMAP pixel and the averaged $T_f$ at each corresponding flux tower site (SMAP mean $T_f$ minus site mean $T_f$).

## Supplementary Files

This is a list of supplementary files associated with this preprint. Click to download.

- CEESIfinal.pdf